nature communications

Article | Article in Press

https://doi.org/10.1038/s41467-026-79386-9

Highly conductive halide Na-ion conductor enabled by cost-effective aliovalent carbonate polyanion substitution for all-solid-state sodium batteries

Received: 30 September 2025

Accepted: 15 October 2026

Published online: 16 November 2026

Check for updates

Xiaolin Guo[1], Man Chen[1], James Burrow[2,3], Santosh Thapa[4], Mahadeen Nashiru[2], Thomas S. Marchese[2,3], Islamiyat Ojelade[5], Yan Chen[6], Sean Holmes[5], Rongfu Zhang[5], Jue Liu[6], Yan-Yan Hu[5,7], Yang-Tse Cheng[4,8], Y. Shirley Meng[2,3] ✉ & Hui Wang[1,9] ✉

Halide-based Na-ion conductors have attracted intense attention due to their favorable (electro)chemical compatibility with oxide positive electrodes. Among these, zirconium (Zr)-based halide solid electrolytes (SEs) offer a cost advantage over halide SEs based on rare metals, but the relatively low ionic conductivity has limited their application in all-solid-state batteries (ASSBs). Here, we report employing soda ash (Na_2CO_3) as a low-cost precursor to introduce an aliovalent carbonate polyanion and produce a family of Na-Zr-Cl-CO_3 conductors with nominal compositions of (2-x)NaCl-$x$$Na_2CO_3$-$ZrCl_4$. This substitution increases structural disorder and amorphization, creating structural environments that facilitate Na^+ transport. At the optimal composition, its ionic conductivity reaches 1.02 mS cm^{-1} at 25 °C. The optimized Na-Zr-Cl-CO_3 SE also exhibits stable electrochemical behavior and favorable mechanical properties. When paired with $NaCrO_2$ positive electrode, the assembled ASSBs deliver an initial discharge capacity of 117 mAh g^{-1} at 0.1 C and demonstrate a long-term cycling stability at 0.3 C for 850 cycles. This work highlights carbonate polyanion substitution as a practical strategy for improving low-cost Zr-based halide SEs, offering a promising route toward ASSBs with high performance.

Solid-state Na-ion conductors are emerging as solid electrolytes (SEs) for all-solid-state batteries (ASSBs) to achieve enhanced safety and more affordability[1,2]. Ideally, SE materials are expected to possess the features of high ionic conductivity and great compatibility to electrode materials. To date, several types of inorganic SE materials (e.g., oxides, sulfides and halides), have been explored and demonstrated to have feasibility in solid-state Na batteries[3–5]. Similar with oxides and sulfide-type SEs, the development of halide-based

[1]Mechanical Engineering Department, University of Louisville, Louisville, KY, USA. [2]Pritzker School of Molecular Engineering, The University of Chicago, Chicago, IL, USA. [3]Energy Storage Research Alliance, Argonne National Laboratory, Lemont, IL, USA. [4]Department of Physics and Astronomy, University of Kentucky, Lexington, KY, USA. [5]Department of Chemistry, Florida State University, Tallahassee, FL, USA. [6]Neutron Scattering Division, Oak Ridge National Laboratory, Oak Ridge, TN, USA. [7]Center of Interdisciplinary Magnetic Resonance, National High Magnetic Field Laboratory, Tallahassee, FL, USA. [8]Department of Chemical and Materials Engineering, University of Kentucky, Lexington, KY, USA. [9]Conn Center for Renewable Energy Research, University of Louisville, Louisville, KY, USA. ✉e-mail: shirleymeng@uchicago.edu; h.wang@louisville.edu

conductors starts from lithium-ion (Li-ion) conductors. Since 2018, halide-based conductors such as Li_3MCl_6 (M = Y, In), and Li_2ZrCl_6 have emerged and quickly gain lots of attention owing to their great ionic conductivity (10^{-4}–10^{-2} S cm^{-1}), high oxidation stability and great processability[6,7].

Halide-type Na-ion conductors were developed later than their Li-ion counterparts and initially exhibited relatively lower ionic conductivity (e.g., 10^{-5} S cm^{-1}). For instance, Na_3YCl_6 was initially reported to have a poor conductivity of 9.5×10^{-8} S cm^{-1} at RT, three orders of magnitude lower than that of its Li-ion counterpart (Li_3YCl_6, 5.1×10^{-4} S cm^{-1})[8,9]. Later, other halide-based conductors were also explored, such as Na_3MCl_6 (M^{3+} = In, Er)[9–11], Na_2ZrCl_6[12], $NaMCl_6$ (M^{5+} = Nb, Ta)[13], $NaAlCl_4$[14]. Among them, $NaNbCl_6$ and $NaTaCl_6$ show high Na-ion conductivity of 10^{-3} S cm^{-1} at 30 °C[13]. In halide-based Na-ion conductors, recent studies have demonstrated that Na^+ transport is strongly governed by local structural features, such as vacancy concentration, Na coordination environment, anion sublattice distortion, and short-range disorder, etc[15,16]. Doping strategies (e.g., partial substitution of metal cations) are effective approaches to modify the local environment. For example, ball-milled $Na_{1-x}La_{1-x}Zr_xCl_4$ with Zr^{4+} partially substitutes for La^{3+}, exhibits lattice expansion and increased lattice parameter, achieving an ionic conductivity of 2.9×10^{-4} S cm^{-1} at 30 °C[17]. Other cation-doping examples include $Na_{3-x}Y_{1-x}Zr_xCl_6$[9], $Na_{2.25-x}Y_{0.25}Zr_{0.75}Cl_{6-x}$[18], $Na_{3-x}Er_{1-x}Zr_xCl_6$[10] and $Na_{2.25}Yb_{0.25}Zr_{0.75}Cl_6$[19]. In addition to metal cation dopants, anions substitutions have been explored for halide SEs to influence their local structure and ion transport. Oxychlorides such as $NaAlCl_{2.5}O_{7.5}$[20] and $0.5Na_2O$-$TaCl_5$[21] form superionic glass to achieve high ionic conductivity ($1–4 \times 10^{-3}$ S cm^{-1}) due to local disordering around Na and open framework. Additionally, the application of dual anions (O^{2-}, Cl^-) increases structural disorder in $NaMOCl_4$ (M = Ta, Nb), which exhibit only weak long-range order with a wide distribution of local Na coordination and orientational disorder of the polyhedral anion sublattice, associated with conductivity of $1.2–1.5 \times 10^{-3}$ S cm^{-1} [22]. Further, ternary systems of NaCl-$TaCl_5$-Ta_2O_5 consisting of NaCl/Ta_2O_5 nanocrystals and amorphous Na-Ta-Cl-O phase exhibits enhanced ionic conductivity of 2.5×10^{-3} S cm^{-1} due to amorphous phase and proposed surface charge effects[23]. The glassy oxyhalide material with fast Na^+ dynamic is also reported in Na_2O-$NaTaCl_6$ (4.41×10^{-3} S cm^{-1})[24]. Moreover, $TaCl_5$–$0.5Na_2CO_3$ with Ta-centered polyhedral embedded in a disordered amorphous matrix displays high ionic conductivity of 5.01×10^{-3} S cm^{-1} [25].

Low-cost halide Na-ion conductors such as Na_2ZrCl_6 which do not contain rare earth elements (Y, Er, Nb, etc.) are more attractive for affordable solid-state Na batteries in practical applications. In 2021, Na_2ZrCl_6 was reported to exhibit an ionic conductivity of 1.8×10^{-5} S cm^{-1} (30 °C), demonstrating its feasibility in ASSBs[12]. Cation incorporation represents an efficient strategy to enhance the ionic conductivity. For example, $Na_{2.25}Y_{0.25}Zr_{0.75}Cl_6$ exhibits enhanced ionic conductivity of 6.6×10^{-5} S cm^{-1} due to the creation of Na vacancies and cooperative MCl_6 octahedral rotation[9]. Further tuning of the NaCl precursor content in $Na_{2.25-x}Y_{0.25}Zr_{0.75}Cl_{6-x}$ ($1.375 < x < 2$) produces NaCl-deficient compounds with mixed nanocrystalline and amorphous phases, leading to a maximum conductivity of 4×10^{-4} S cm^{-1} [18]. $Na_{3-x}Er_{1-x}Zr_xCl_6$ achieves an ionic conductivity of 4×10^{-5} S cm^{-1} at $x = 0.6$ due to slightly expansion of $NaCl_6$ polyhedral volume[10]. In addition to cation doping, anion substitution to Zr-based halides has been explored. For instance, ZrO_2-incorpated Na_2ZrCl_6 exhibits an ionic conductivity of 1.1×10^{-4} S cm^{-1} [26], while Na_2O_2-$ZrCl_4$ compounds and S-doped Na_2ZrCl_6 show improved ionic conductivity of 4.1×10^{-4} S cm^{-1} [21], and 7.5×10^{-4} S cm^{-1} [27]. Through the mixing of multiple anions (F, Cl) and tuning Na concentration, a distorted and distorted anion structure is obtained in $Na_{0.5}ZrCl_4F_{0.5}$ (1.12×10^{-4} S cm^{-1})[28]. Despite this important progress, it is still challenging to realize a high ionic conductivity (10^{-3} S cm^{-1}) for Zr-based halides with low material costs and long-term stability in ASSBs.

In this work, we report the synthesis of a halide-type Na-Zr-Cl-CO_3 compound by utilizing soda ash as a low-cost precursor to introduce polyatomic carbonate anions into the NZC family of conductors. With the 1:1 mole ratio of NaCl and Na_2CO_3, a high ionic conductivity of 1.02×10^{-3} S cm^{-1} at 25 °C is achieved for Zr-centered halide family of SEs, significantly higher than that of pristine NZC (2×10^{-5} S cm^{-1}). With these low-cost precursors, the estimated material cost for Na-Zr-Cl-CO_3 compounds is about $7.61/kg (based on quantity-price model, Table S1). In addition, the assembled Na-Sn||$NaCrO_2$ ASSBs show an initial specific capacity of 117 mAh g^{-1} at 0.1 C, and stable electrochemical cycling at 0.3 C for 850 cycles at 25 °C with 78% capacity retention. This work highlights exploring highly conductive halide Na-ion conductors with diverse compositions, with the aim of paving pathways for the development of high-performance ASSBs.

Results and discussion

Synthesis and structure characterization of NZC-yCO compounds

Na_2ZrCl_6 (NZC), a baseline halide, was synthesized through the mechanochemical reaction of NaCl and $ZrCl_4$ (mole ratio of 2:1). To that base, Na_2CO_3 was introduced to partially substitute NaCl reactant with a fixed ratio to produce a series of (2-x)NaCl-xNa_2CO_3-$ZrCl_4$ compounds, (x = 0.25, 0.5, 0.75, 1.0 and 1.5), here referred to as NZC-yCO (y = 100x). For instance, NZC-100CO refers to NaCl-Na_2CO_3-$ZrCl_4$ with x = 1.0. Figure 1a shows X-ray diffraction (XRD) patterns for synthesized samples with different contents of carbonate anion incorporation using Mo Kα radiation (λ=0.709 Å). Pristine NZC exhibits polymorphism, consisting of a dominant trigonal phase (space group P$\bar{3}$m1) and a minor monoclinic phase (space group P21/n), as confirmed by Rietveld refinement (Supplementary Fig. 1, Supplementary Table 1) and in good agreement with previous reports[9,12,15]. Na atoms occupy octahedral sites in the trigonal structure, whereas prismatic sites appear only in the monoclinic phase. When introducing a small amount of Na_2CO_3 content, the trigonal structure remains in NZC-25CO sample. However, as the content of carbonate increases, a series of diffraction patterns appear at 2θ = 14.8, 20.5 and 26°, accompanying by a decrease in the intensity of the NZC diffraction peaks. These patterns cannot be assigned to polymorph NZC ($P2_1/n$)[15] and monoclinic NYZC[9]; but instead likely correspond to cubic NaCl. Additionally, this transition is also evidenced in the XRD patterns of NZC-yCO samples collected using Cu Kα radiation (λ=1.5416 Å), as shown in Supplementary Fig. 2.

Figure 1b displays the neutron diffraction (ND) pattern with Rietveld refinement for the NZC-100CO sample. The high background in ND pattern indicates that an amorphous phase is formed during the mechanochemical synthesis process. Amorphization of Na SEs has been widely reported to enhance Na-ion transport in halide-type SEs[12,29], where fully amorphous materials exhibit higher ionic conductivity than that of annealed samples. In the refinement, the diffraction patterns are ascribed to cubic NaCl with lattice parameter $a = b = c$ = 5.6451(5) Å, and monoclinic Na_2CO_3 with lattice parameter a = 8.9087(9) Å, b = 5.2408(1) Å, c = 6.0493(2) Å (Supplementary Table 2). Unlike the XRD results, Na_2CO_3 peaks are more obvious in ND patterns due to scattering difference, specifically, the higher sensitivity of neutrons to light elements (O, C) compared to X-rays[30]. Furthermore, in-situ ND measurement of the as-synthesized NZC-100CO sample was conducted during heating from 25 °C to 300 °C. (Supplementary Fig. 3) As temperature increases, the diffraction peaks of the cubic phase gradually intensify due to increased crystallization.

The selected area electron diffraction (SEAD) pattern for NZC and NZC-100CO sample are distinct in Fig. 1c. Transmission Electron Microscopy (TEM) images (Supplementary Fig. 4) display submicron-sized particles for both NZC and NZC-100CO samples, respectively.

STEM Scanning Transmission Electron Microscopy X-ray energy dispersive spectroscopy (STEM-EDS) spectral imaging revealed a relatively homogeneous elemental distribution of O and C elements across the NZC-100CO particle, lacking any clear agglomeration of Na_2CO_3 or NaCl byproduct (Fig. 1d). These observations are consistent with production of a uniform nanocomposite comprised of an amorphous mixed-anion (CO_3^{2-}/Cl^-) matrix supporting Na_2CO_3 and NaCl nanocrystals. Based on three characterization tools (XRD, SEAD, ND), the d-spacing values are observed to be consistent (Supplementary Fig. 5), which further confirms the structural difference between NZC-100CO and pristine NZC sample.

Surface chemistry and chemical environment

To probe the local Na^+ environments, ^{23}Na solid-state nuclear magnetic resonance (SS-NMR) spectroscopy was performed on a series of NZC-CO samples. As shown in Fig. 2a and Supplementary Table 3, the pristine NZC exhibits strong features associated with octahedral (0.1, −6.3 ppm) and prismatic (−11.4 ppm) local environments, with an additional minor peak associated with Na-Cl (7.3 ppm), in agreement with previous literature[9,15]. At low carbonate incorporation (NZC-25CO), two octahedral Na environments are retained alongside a slight increase in the Na-Cl peak. Importantly, the prismatic features associated with pristine NZC disappear with the emergence of a resonance at −8.3 ppm, assigned to the Na-Zr-Cl-CO_3 local environment. As the carbonate content increases, the octahedral Na signals gradually weaken, whereas the intensity of Na-Zr-Cl-CO_3 and Na-Cl peaks progressively increase in intensity. In NZC-100CO sample, only two resonances at −8.8 ppm and 7.3 ppm remain, indicating complete disappearance of the NZC phase, in agreement with the XRD, ND, and SEAD results. The NaCl content was quantified from the NMR spectra using an external NaCl standard. The NZC-100CO sample is estimated to consist of 90 wt% Na-Zr-Cl-CO_3 compound and 10 wt% NaCl. In addition, the absence of a resonance corresponding to Na_2CO_3 at ~5 ppm (Supplementary Fig. 6), suggests that only a minimal amount of Na_2CO_3 is present, in agreement with the XRD results. The Na resonance at 8–9 ppm has also been reported in other anion-doped halides and is attributed to Na^+ in highly coordinated local environment[31,32]. The NMR results reveal a change of local environment for Na^+ sites ascribed to the incorporation of carbonate anion in NZC-yCO samples. Figure 2b displays the thermogravimetric analyzer (TGA) curves of NZC and NZC-100 CO samples to examine the thermal stability. The NZC shows thermal stability until 400 °C and then experiences a decomposition reaction (400–560 °C)[33]. For the NZC-100CO sample, a slight weight loss (10 wt%) at 180–230 °C that is attributed to the decomposition of carbonate groups in the Na-Zr-Cl-CO_3 compound, followed by a large weight loss above 400 °C due to further decomposition reaction.

The surface chemistry for NZC-100 CO and NZC samples was characterized by X-ray photoelectron spectroscopy (XPS). As plotted in Fig. 2c, d, the incorporation of carbonate anion causes more obvious changes for the C 1*s* spectrum than Zr 3*d* and Cl 2*p* spectra for NZC-100 CO sample, in comparison with that of NZC sample. In the C 1*s* spectrum, NZC-100CO sample displays a peak located at 290.5 eV that corresponding to $(CO_3)^{2-}$ group[34,35], (also confirmed by XPS of Na_2CO_3 in Supplementary Fig. 7), while this peak is absent in NZC sample. Additionally, the Zr 3*d* and Cl 2*p* spectra are almost identical for NZC-100 CO and NZC samples, both of which exhibit strong Zr $3d_{5/2}$ peaks and Cl $2p_{3/2}$ peaks, indicate that the incorporation of carbonate does not dramatically influence Zr local environment or reduce its oxidation state. In the FTIR spectra for a series of NZC-CO samples (Supplementary Fig. 8), additional peaks emerge at 1426 and 868 cm^{-1} and become stronger after introducing carbonate anion. These peaks are ascribed to the C-O stretching and C=O bending bonds from carbonate $(CO_3)^{2-}$ group, although there is a slight left shift compared to Na_2CO_3. Meanwhile, the peak at 769 cm^{-1} that comes from NZC also remained in NZC-CO samples.

Neutron total scattering and pair distribution function (nPDF) analysis were performed on NZC-100CO and NZC samples to

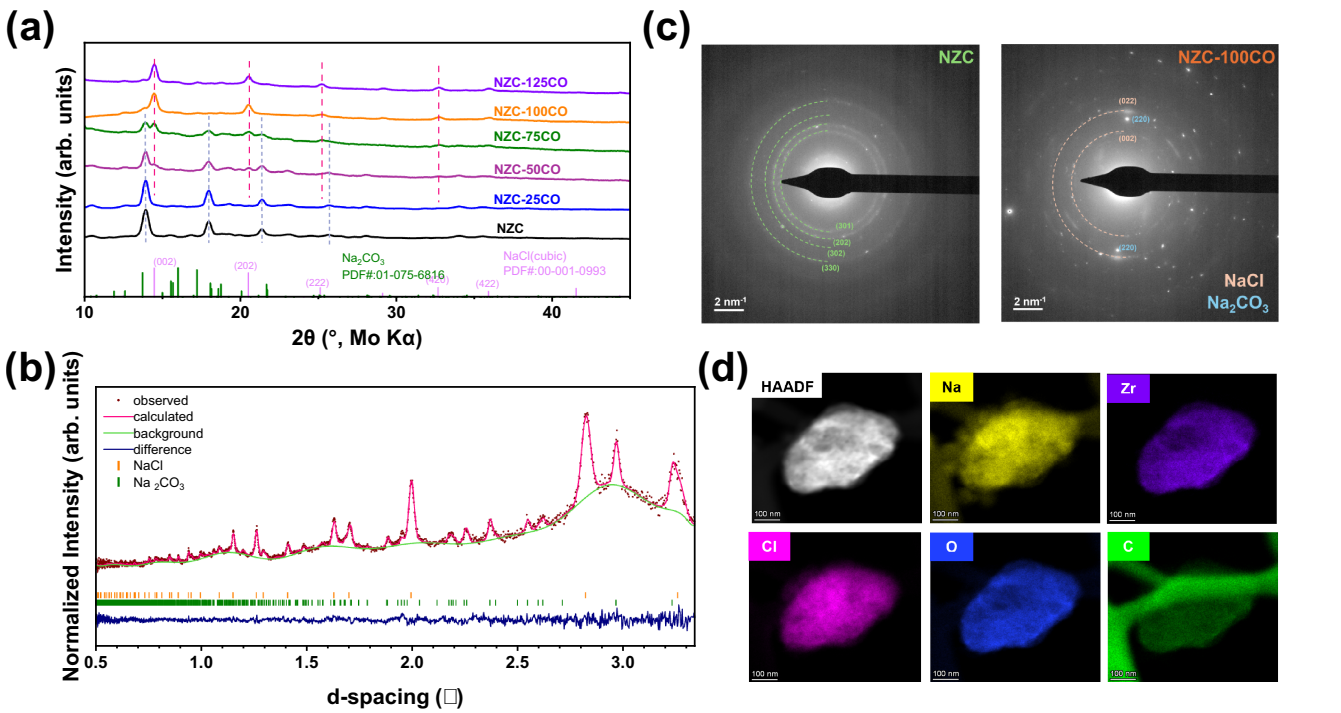


Fig. 1 | Structural and morphology characterization of NZC-yCO. a XRD patterns (Mo source) of NZC-yCO samples (y = 0, 25, 50, 75, 100, 125). **b** Neutron diffraction pattern of as-synthesized NZC-100CO. **c** SAED pattern of NZC and NZC-100CO. **d** STEM + EDS spectral imaging of NZC-100CO (Na, Zr, Cl, O, C). Notably, dark green comes from the sample while bright green is from the carbon mesh on TEM grid.

https://doi.org/10.1038/s41467-026-79386-9

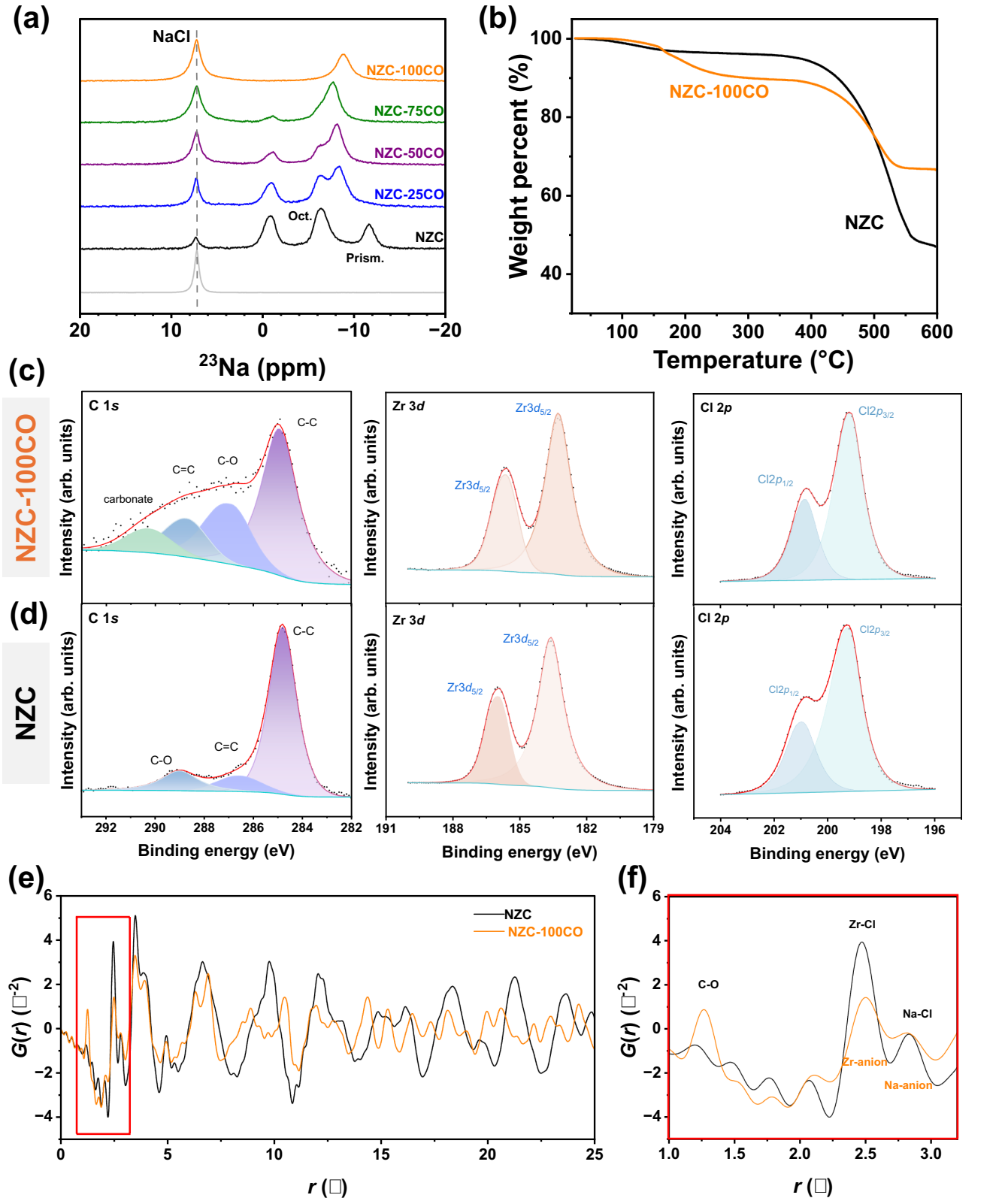


Fig. 2 | Local and surface environment characterization of NZC-yCO. a ^{23}Na SS-NMR spectra for NZC-yCO samples (y = 0, 25, 50, 75, 100). **b** TGA curves of NZC and NZC-100CO from 25 °C to 600 °C under N_2 flow. XPS spectra of **c** NZC-100CO sample and **d** NZC sample with C1s, Zr 3 d and Cl 2p high-resolution scans. **e** Reduced neutron pair distribution function (nPDF, G(r)) patterns of NZC and NZC-100CO. **f** Enlarged view of the low-r region between 1.0 and 3.2 Å highlighted in (**e**) with corresponding atomic pairs inserted.

investigate their local structure (Fig. 2e). NZC-100CO shows strongly damped correlations beyond 8 Å, confirming the loss of long-range crystalline order, while the retained short-range features indicate the local coordination motifs are preserved. Because NZC-100CO also contains crystalline NaCl, the amorphous contribution was isolated by subtracting the NaCl signal (obtained from a Rietveld refinement of NaCl alone in Q-space) from normalized distinct neutron scattering structure factor S(Q)-1, and the sine Fourier transforming the resulting residual (Supplementary Figs. 9 and 10). The isolated amorphous G (r) decay toward the average pair-correlation density beyond 8 Å, confirming that the long-range disorder originates from the amorphous phase. Notably, in the short-range regime, a characteristic peak near 1.26 Å (consistent with C-O bond distance in carbonate species) provides structural evidence for carbonate incorporation into the NZC-100CO framework. Moreover, in the total n-PDF (Fig. 2f), the Na-Cl correlation at 2.83 Å is markedly broadened, indicating a wide bond-length distribution. The phase-isolated amorphous G(r) shows a similar set of correlations to pristine NZC (Supplementary Fig. 11) but with slight differences: the Na-anion and Zr-anion correlations are broadened, and the Zr-anion distance is slightly increased. This confirms that this distorted, partially undercoordinated Na environment originates from the amorphous phase. This structural heterogeneity suggests modified polyhedral connectivity with partially undercoordinated Na sites[36], which are expected to reduce Na^+ migration barriers and facilitate fast ion transport in NZC-100CO. Such short-range disorder-driven conduction is consistent with recent reports on mixed-anion halide systems[36–38].

Ionic conductivity and mechanical properties for NZC-yCO samples

Electrochemical impedance spectroscopy (EIS) was employed to examine the conductive properties of NZC-yCO SEs. Figure 3a shows the ionic conductivity and activation energy depending on the anion incorporation contents. NZC shows an ionic conductivity of 3.2×10^{-5} S cm^{-1} at 25 °C, which is comparable with previous reports (2×10^{-5} S cm^{-1})[12]. As the carbonate anion content increases, the variation of ionic conductivity for NZC-yCO samples displays a volcano shape, initially increasing with carbonate incorporation and then decreasing beyond the optimal content ($y = 100$). The decreased ionic conductivity results from increased content of NaCl byproduct, as confirmed by XRD and NRM results. The high-frequency impedance in Nyquist plots (Fig. 3b) also reflects this trend accordingly. Among NZC-yCO samples, NZC-100CO reaches a maximum ionic conductivity of 1.02×10^{-3} S cm^{-1} at 25 °C, which is about 30-fold higher than that of pristine NZC sample (3.2×10^{-5} S cm^{-1}).

To gain deeper insight into the origin of high ionic conductivity in NZC-100CO, ^{23}Na T_1 relaxation and variable-temperature NMR (VT-NMR) measurements were performed to probe Na^+ dynamics, together with ^{13}C magic-angle spinning (MAS) NMR to characterize the incorporated carbonate. ^{23}Na SS-NMR T_1 measurements (Table 1) show that the amorphous Na-Zr-Cl-CO_3 compound (−8.8 ppm) exhibits a relaxation time of 0.0039 s, more than two orders of magnitude shorter than that of Na-Cl (1.29 s), indicating substantially faster Na^+ dynamics within the amorphous phase. VT-NMR measurements (Supplementary Fig. 12) further reveal that the amorphous component (Na-Zr-Cl-CO_3) passes through a clear T_1 minimum near 35 °C, the characteristic signature of the intermediate motional regime ($\omega_0\tau_c = 1$), from which the Na^+ motion rate of $1/\tau_c = 5 \times 10^8$ s^{-1} ($\omega_0 = 79.35$ MHz). In contrast, the NaCl resonance shows monotonically decreasing T_1 with temperature, characteristic of thermally activated motion in the slow-motion regime ($\omega_0\tau_c \gg 1$). Furthermore, a progressive downfield shift of the amorphous Na-Zr-Cl-CO_3 resonance with temperature provides independent confirmation on enhanced Na-ion dynamics through motional averaging the quadrupolar coupling[39,40]. In addition, ^{13}C MAS NMR of ^{13}C-enriched NZC-100CO sample resolves a major resonance at 171 ppm, assigned to carbonate incorporated within amorphous Na-Zr-Cl-CO_3 framework (Supplementary Fig. 13), and consistent with the C-O correlation peak at 1.26 Å (from CO_3^{2-}) in the nPDF. These observations confirm that carbonate incorporation is the chemical driver of structural disorder.

Combining the nPDF, VT-NMR, and ^{13}C MAS NMR results, a coherent mechanism for fast Na^+ transport in NZC-100CO emerges: mechanochemical incorporation of carbonate disrupts the long-range crystalline periodicity while largely preserving the local Na coordination motif, generating locally distorted and partially undercoordinated Na sites[36], as evidenced by much broadened Na-Cl correlation peak in the nPDF analysis. These disordered local environments facilitate rapid Na^+ motion and ultimately lead to high ionic conductivity of NZC-100CO. NaCl exhibits slow dynamics, and Na_2CO_3 is below the detectable limit of both SS-NMR and XRD; neither phase contributes significantly to the ionic conductivity, although amorphous-crystalline interfaces may partially assist local ion migration[28]. Consistently, post-annealing NZC-100CO sample at 200 °C for 6 h increases crystallinity (Supplementary Fig. 14) yet dramatically raise the impedance (Supplementary Fig. 15), further highlight the important role of structural disorder in fast ion transport. Figure 3c shows linear behavior in Arrhenius plots for NZC-CO samples within the temperature range of 30–70 °C. NZC-100CO sample shows an activation energy of 0.293 eV, substantially lower than that of NZC (0.4 eV), indicating reduced Na^+ site binding energy within the disordered mixed-anion framework. In addition, the electronic conductivity of NZC-100CO is estimated to be 6.21×10^{-11} S cm^{-1} by direct polarization (Fig. 3d), while other samples such as NZC, NZC-25CO, NZC-50CO and NZC-75CO also mention low electronic conductivity at 10^{-11} S cm^{-1} level (Supplementary Fig. 16).

Nano-indentation experiments were employed on cold-pressed pellets of NZC-yCO samples to examine their mechanical properties, including the elastic modulus (E) and hardness (H). In the experimental setup (the inset of Fig. 3e), the measurements were conducted inside a glovebox under an Ar environment using a three-sided diamond pyramidal Berkovich indenter tip; for each pellet, 16 measurements were performed to collect data for analysis. Supplementary Fig. 17 displays the average load-displacement curves for NZC, NZC-25CO, NZC-50CO and NZC-100CO samples. The elastic modulus and hardness calculations are based on the Oliver-Pharr method[41]. As load values increases, the displacement continuously increases for all samples. During all measurements, no obvious pores and cracks appeared in magnified optical images (Supplementary Fig. 18), indicating the ductile feature of the sample pellets.

Figure 3e presents the variation of elastic modulus and hardness dependent on carbonate anion content in NZC-yCO samples. For pristine NZC, the average elastic modulus value is 8.5 ± 0.4 GPa, with a hardness value for NZC of 0.34 ± 0.03 GPa. When the anion content increases, both the modulus and hardness values gradually increase. NZC-100CO sample exhibits an elastic modulus value of 13.0 ± 0.6 GPa and hardness of 0.48 ± 0.04 GPa. The elastic modulus values for different types of SE materials are compared in Fig. 3f. The sources of the literature data are listed in Supplementary Table 4. The mechanical properties of NZC-100CO are comparable with other halide-type SEs (14–17 GPa)[42] and slightly higher than that of borohydrides (8–12 GPa)[43], while obviously lower than that of sulfide-type (20–32.2 GPa)[44,45] and oxide-type SEs (64–150 GPa)[46–48]. Compared to stiffer SE materials, the softer mechanical properties of NZC-yCO samples may release stress through elastic-plastic deformation, mitigating stress concentration and preventing electro-chemo-mechanical failure. In addition, the creep measurements (Supplementary Fig. 19) show that the NZC-100CO sample exhibits significant time-dependent deformation under constant stress compared with pristine NZC. This creep deformation allows NZC-100CO sample to accommodate the volume change of positive active materials and

https://doi.org/10.1038/s41467-026-79386-9

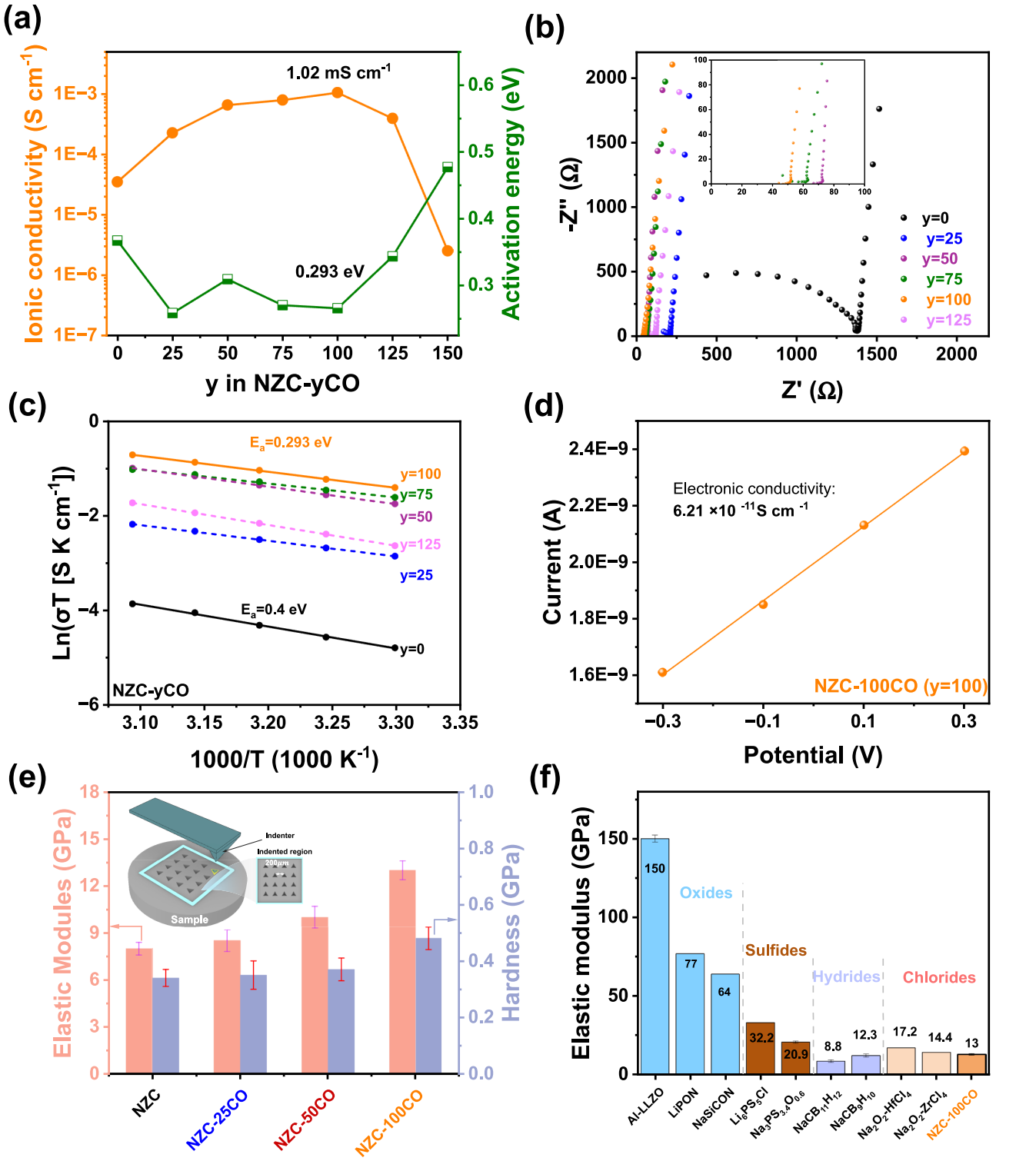


Fig. 3 | Sodium ion, electron transport and mechanical measurements of NZC-yCO samples. a Ionic conductivity and activation energy of NZC-yCO ($0 \le y \le 150$) samples dependent on the composition. **b** Nyquist plot of NZC-yCO ($0 \le y \le 125$) measured at 25 °C. **c** Arrhenius plot of NZC-yCO ($0 \le y \le 125$) in the temperature range of 30–70 °C. **d** The fitting line of equilibrium current response at different applied polarization voltages for electronic conductivity for NZC-100CO sample. **e** The Elastic modulus and hardness of NZC-CO samples. Sixteen measurements were performed for each sample, with the values with error bar represent the average value with standard derivation, respectively. **f** Comparison of Elastic modulus of NZC-100CO with other reported solid electrolytes. The source of the literature data shown in (**f**) can be found in Supplementary Table 4.

Table 1 | T_1 relaxation measurement of NZC and NZC-100CO

T_1 relaxation (s)				
Sample	Na-Cl	Site 1	Site 2	Site 3
NZC (Pristine)				12.34
0.77	0.50			0.25
NZC-100% CO	1.29	-	-	
0.0039				

maintain good interfacial contact between SE and electrode during cycling. Consequently, its compliance and creep-enabled deformation promote intimate particle-electrolyte contact and suppress interfacial void formation, leading to enhanced long-term electrochemical stability[49,50].

Electrochemical performance of NZC and NZC-100CO SE

Linear sweep voltammetry (LSV) was employed to examine the electrochemical stability window for both oxidation and reduction reactions (Supplementary Fig. 20). The base NZC sample exhibits an oxidation decomposition at 3.9 V vs. Na^+/Na-Sn alloy (4.2 V vs. Na^+/Na). After introducing CO_3^{2-} anion, NZC-100CO sample shows a comparable oxidation potential of 3.8 V vs. Na^+/Na-Sn alloy (4.1 V vs. Na^+/Na). On the reduction side, the LSV curves confirm that NZC-100CO begin to decompose at a reductive potential of 1.3 V while that value for NZC of 1.2 V vs. Na^+/Na-Sn alloy. The comparisons of LSV results indicate that the NZC-100CO sample (with ionic conductivity of 1.02 mS cm^{-1}) retains a wide electrochemical window of 1.3–3.8 V for oxidation and reduction stability, enabling application as catholyte for layered transition metal oxide positive electrodes.

The ASSBs structure is illustrated in Fig. 4a, in which NZC-100CO and pristine NZC are used as the SE materials, and $NaCrO_2$ (NCO) is chosen as the CAM, and Na_3PS_4 (NPS) is introduced as an anolyte between the SE and the Na-Sn alloy negative electrode. The Na_3PS_4 was synthesized through mechanochemical process (specifically, ball milling for 5 h and heat treatment at 270 °C), and its ionic conductivity is around 2×10^{-4} S cm^{-1} at 25 °C (Supplementary Fig. 21). The XRD patterns of a mixture of NPS and NCO-100CO in Supplementary Fig. 22 clearly show the characteristic patterns for the individual materials without crystalline byproducts, suggesting good chemical compatibility between each other. The ASSBs with structure of Na-Sn | NPS|SE|NCO (SE refers to NZC-100CO and NZC samples) were cycled between 2.0 and 3.4 V. The active material loading was 5.05 mg cm^{-2}, and the theoretical capacity loading is 0.606 mA h cm^{-2}.

Figure 4b compares the initial discharge/charge profiles for the ASSBs employed with different SEs and cycled at 0.1 C (1 C = 120 mA g^{-1}). When using pristine NZC as SE, an obvious polarization in the voltage profiles is observed, leading to an initial discharge capacity of 105 mAh g^{-1}. In contrast, the cell with NZC-100CO SE displays a high initial discharge capacity of 117 mAh g^{-1}, a columbic efficiency of 97% and reduced polarization. As shown in Fig. 4c, the dQ/dV profile for the initial cycle in NZC-100CO based cell displays three sharp oxidation peaks (2.85, 2.99, 3.22 V) and reduction peaks (3.15, 2.79, 2.73 V), corresponding to the de-sodiation and sodiation of $NaCrO_2$ during the charge/discharge process[51,52]. However, for the NZC-based cell, only one broad pair of oxidation/reduction peaks (2.94/2.68 V) are observed, suggesting large kinetic polarization due to insufficient ion conductivity in NZC. The EIS comparison of ASSBs using two SEs (Fig. 4d) shows that the cell with NZC–100CO exhibits significantly lower impedance than the NZC-based cell both before and after cycling. Equivalent circuit fitting (Supplementary Fig. 23) indicates the lower values of bulk resistance (R_1), interfacial resistance (R_2) and charge transfer resistance (R_3) for NZC–100CO-based cell than that of NZC-based cell. (Supplementary Table 5) The reduced resistance is attributed to two factors: the high conductivity of NZC-100CO as a catholyte, enhancing Na^+ transport in the composite positive electrode; and its creep-enabled deformation, which maintains intimate contact between the SE and positive electrode during cycling. Figure 4e illustrates the rate-performance of NZC-100CO based cells. At 0.1 C, the cell delivers a capacity of 115 mAh g^{-1}, The capacity slightly decreases to 106 mAh g^{-1} for 0.2 C, 104 mAh g^{-1} for 0.3 C and 99.8 mAh g^{-1} for 0.5 C, respectively. When the cell cycles at 1 C, its discharge capacity remains at 85.3 mAh g^{-1}. After returning to a low C-rate at 0.1 C, the capacity returns to 106 mAh g^{-1}. This observation indicates a good rate capability of NZC-100CO based ASSBs.

The long-term cycling performance of ASSBs with NZC-100CO and NZC SEs are displayed in Fig. 4g. For the NZC-100CO cell, after the initial 3 cycles under 0.1 C, there is a slight capacity drop from 116 to 113 mA h g^{-1} for the 4th cycle, followed by highly stable cycling performance. Conversely, the NZC-based cell displays poor cycling performance with a low specific discharge capacity around 60 mAh g^{-1} at 0.3 C. The ASSBs with NZC-100CO SE displays a specific discharge capacity of 101 mAh g^{-1}, 95 mAh g^{-1}, and 90 mAh g^{-1} after 100, 200, and 400 cycles, respectively. After 850 cycles, the capacity remains at 85 mAh g^{-1} and the average CE value is 99.97%. Compared with the NZC-based cell, ASSBs employing NZC-100CO SE exhibit significantly improved cycling stability, which can be attributed to its enhanced ability to accommodate volume changes, as evidenced by the creep measurement results (Supplementary Fig. 19). Figure 4f shows discharge/charge profiles for the NZC-CO based ASSBs under 0.3 C at 1st, 100th, 200th, 300th, 500th, and 700th cycle within the electrochemical window of 2.0–3.4 V. Obvious oxidation and reduction peaks appear for these cycles in the dQ/dV profiles at 0.3 C (Supplementary Fig. 24).

The material cost of NZC-yCO samples was also estimated and compared with other halide-type Na-ion conductors. The preliminary material cost was calculated using a method proposed by Hart[53] for the bulk prices of precursors, using a correlation between price P and quantity Q: $\log_{10}P = \log_{10}a + b\log_{10}Q$, where P is unit price ($/kg) and Q is the purchase quantity (g). The details about the bulk price precursors are provided in Supplementary Table 6. In addition, the SEs cost (Supplementary Table 7) was calculated based on the reported synthesis route and bulk prices of precursors estimated earlier. According to Fig. 4h, the raw materials cost of NZC-100CO in this work is only about $7.61/kg (even lower than $8.48/kg for NZC) but achieves a high ionic conductivity of 1.02×10^{-3} S cm^{-1} at 25 °C[9,10,12,14,17–19,26,29,42,54–59]. The source of the literature data shown in Fig. 4h can be found in Supplementary Table 8. To date, this material exhibits high ionic conductivities reported for Zr-based Na-ion conductors while also possessing a low raw material cost among all other reported Na-based halide superionic conductors with decent ionic conductivity (>10^{-4} S cm^{-1}). The combination of cost-competitiveness and high ionic conductivity makes carbonate-incorporated NZC a highly promising SE candidate for application in ASSBs.

In summary, a family of Zr-based halide Na-ion conductors (Na-Zr-Cl-CO_3 compounds) that utilize a low-cost precursor (soda ash) to introduce polyanions into Na_2ZrCl_6 was designed and synthesized through a mechanochemical approach. With the optimal ratio of NaCl to Na_2CO_3, the NaCl-Na_2CO_3-$ZrCl_4$ (NZC-100CO) sample exhibits an ionic conductivity of 1.02 mS cm^{-1}, which is a high value among other Zr-centered halide Na-ion conductors. In addition, the materials cost for NZC-100CO is estimated to be about $7.61/kg, significantly lower than other halide-based SEs. The assembled ASSBs display an initial discharge capacity of 117 mAh g^{-1} at 0.1 C and demonstrate stable long-term cycling stability at 25 °C for 850 cycles at 0.3 C with an average CE value of 99.97%. This work highlights utilizing low-cost

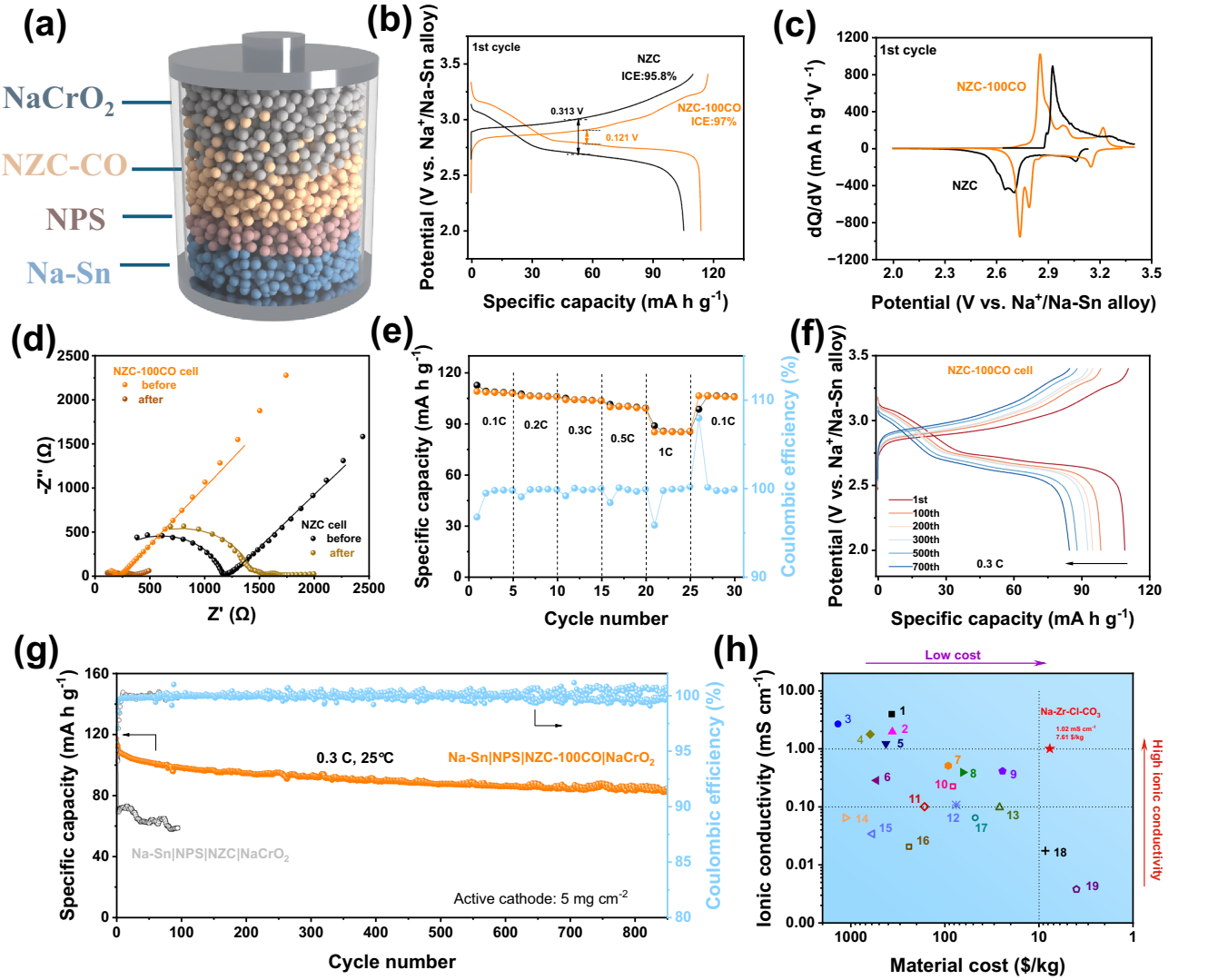


Fig. 4 | Electrochemical performance of NZC−100CO in all-solid-state batteries. **a** The structure illustration of assembled ASSBs. **b** Initial charge/discharge curves at 0.1 C and **c** initial capacity differential (dQ/dV) curves of ASSBs with NZC and NZC−100CO solid electrolytes. **d** EIS Nyquist plots of ASSBs with NZC-100CO and NZC SEs before and after cycling. **e** the rate-performance (0.1, 0.2, 0.3, 0.5 and 1 C). The C-rate was calculated based on 1 C = 120 mA g^{-1}. **f** The charge/discharge curves of ASSB with NZC-100CO under 0.3 C at 1st, 100th, 200th, 300th, 500th, 700th cycle; **g** the long-term cycling performance under 0.3 C of ASSB with NZC-100CO and NZC SE at 25 °C. (active material loading 5 mg cm^{-2}). **h** Comparison of materials cost and ionic conductivity of NZC−100CO and reported sodium-based halide solid electrolytes. The source of the literature data shown in (**h**) can be found in Supplementary Table 8.

precursors to synthesize Zr-based halide Na-ion conductors with boosted ionic conductivity, thereby offering valuable insights into the development of advanced solid ionic conductors for ASSBs.

Methods

Materials synthesis

All synthesis procedures were conducted under inert argon gas atmosphere. The *(2-x)*NaCl-*x*Na_2CO_3-$ZrCl_4$ ($x = 0$, 0.25, 0.5, 0.75, 1.0 and 1.5) compounds were synthesized with raw materials NaCl (Alfa Aesar, 99%), $ZrCl_4$ (Thermo Scientific Chemicals, 99.5%) and Na_2CO_3 (Sigma-Aldrich, 99.5%) in a stoichiometric ratio. They were mixed in mortar pestle and then loaded in 100 mL milling jar with 8 mm yttrium-stabilized zirconia grinding and ball milled for 10 h. The synthesized *(2-x)*NaCl-*x*Na_2CO_3-$ZrCl_4$ compounds refer to NZC-yCO samples ($y = 100x$), for instance, NZC-100CO sample corresponds to $x = 1.0$, that is NaCl-Na_2CO_3-$ZrCl_4$.

Na_3PS_4 was prepared with Na_2S (Thermo Scientific chemicals, anhydrous) and P_2S_5 (Alfa Aesar, 98%) precursor with a stoichiometric ratio of 3:1 by ball-milling at 500 rpm for 10 h and then sealed under vacuum in a glass tube for annealing at 270 °C for 2 h. Na-Sn alloy was synthesized by mixing sodium metal with tin powder (Thermo Scientific Chemicals, 99.5%). The mixture was ball-milled at 500 rpm for 5 h to synthesize homogeneous negative electrode.

Characterizations

XRD patterns of NZC-yCO samples ($y = 0$, 25, 50, 75, 100, 125) were collected in the 2θ range of 10–45° with a step size of 0.01° using a Bruker X8-Apexll CCD sealed Tube diffractometer equipped with a molybdenum source radiation ($\lambda = 0.7107$ Å) with a 2D area detector. All samples were hermetically sealed in 0.5-mm-diameter boron-rich capillary tubes. Additionally, the NZC-yCO samples were also characterized by X-ray diffraction (ARL EQUINOX 100 X-ray Diffractometer, nickel filtrated Cu Kα radiation, $\lambda = 1.5406$ Å). Kapton films were used to cover samples to avoid air-exposure. The XPS surface measurements were conducted with the Thermo Scientific K-Alpha XPS system, and instrument utilizes a micro-focused, monochromated Al Kα source with a beam energy of 1486.6 eV. The air sensitive samples were transferred from the Ar-filled glovebox to XPS

analysis chamber with an air-free sample holder to prevent the surface contamination. All XPS binding energies were referenced to the C 1 s peak (C-C/C-H) at 284.8 eV.

ND experiments were conducted at VULCAN diffractometer[60], Spallation Neutron Source at Oak Ridge National Laboratory. High-resolution ex-situ ND was performed on as-synthesized NZC-100CO and NZC samples at 25 °C. In situ ND was also conducted on the NZC-100CO sample (as-milled powder loaded in a vanadium can) that placed in a furnace with an inert atmosphere for the heating from 25 °C to 300 °C with a heating rate of 1.5 °C min^{-1}. The ND patterns were continuously collected with 20 Hz chopper and high-intensity guide configuration during the heating process. The in-situ ND data were chopped using VDRIVE software[61]. Rietveld refinement of the diffraction patterns was performed using GSAS and EXPGUI software[62,63]. The diffraction pattern was normalized by using the equation

$$I_{norm}(d) = \frac{I_{\text{sample}}(\text{d})}{I_V(d)}, \quad (1)$$

where $I_{\text{sample}}(\text{d})$ and $I_V(d)$ are the intensity of the sample and the incoherent intensity of vanadium, respectively[64]. Total scattering measurements were performed at the NOMAD beamline (BL-1B) at the Spallation Neutron Sources (SNS) at Oak Ridge National Laboratory (ORNL). The powder samples were loaded into 6 mm vanadium cans in an argon-filled glovebox. For the nPDF data reduction, the structure function S(Q) was Fourier transformed into the reduced pair distribution function, g(r) is the atomic pair distribution function, r is the atomic pair distance, ρ is the atomic number density, Q is the momentum transfer with Q_{min} = 0.5 $Å^{-1}$ and Q_{max} = 20 $Å^{-1}$. The normalized distinct neutron scattering structure factor S(Q)-1 of NZC-100CO was processed using TOPAS-Academic (Version 8) to isolate the amorphous and crystalline (NaCl) contributions. This was achieved by Rietveld refinement (in Q-space) using only the crystalline phase NaCl, the refinement residual is dominated by the diffuse scattering signal from the amorphous components. It is worth noting that thermal diffuse scattering was modeled as the background in Rietveld refinement of the S(Q)-1 data (Supplementary Fig. 9a). More details can be found in the literature[65,66]. The obtained residual data (which mainly contains the scattering signal from the amorphous components) was then Sine Fourier transformed with a Q_{max} of 30 $Å^{-1}$ to obtain the reduced nPDF G(r) for amorphous phase.

$$G(r) = [1 - g(r)]r = \frac{1}{2\pi^2\rho_0}\int_{Q_{\text{min}}}^{Q_{\text{max}}} Q[S(Q) - 1]\sin(Qr)dQ, \quad (2)$$

The sample morphology was examined using an Iliad Ultra scanning transmission electron microscope (STEM; Thermo Fisher Scientific) at Argonne National Laboratory. To minimize air exposure, the prepared TEM grids were loaded into a Simple Origin Model 201 inert-gas-transfer cryogenic TEM holder inside an Ar-filled glovebox, then sealed and directly transferred to the microscope. STEM imaging was performed at an accelerating voltage of 300 kV in high-angle annular dark-field (HAADF) imaging mode. TEM Image and SAED data were collected on the post column Ceta II CMOS 4kx4k and Falcon IVi cameras. EDS spectral images were collected using the UltraX detector. The SAED images were acquired with an electron does rate of ~10 e $Å^{-2}$ s^{-1} for ~1 s Thermal stability of the NZC-yCO samples were measured using Q600 SDT under a nitrogen atmosphere flow (100 mL min^{-1}) from 25 °C to 600 °C with heating rate of 10 °C min^{-1}. Fourier Transform Infrared Spectroscopy (FTIR) were collected via PerkinElmer Spectrum BX FTIR system using excitation laser source of 633 nm in transmission mode.

^{23}Na Magic Angle Spinning (MAS) Nuclear Magnetic Resonance experiments of all NZC-yCO (y = 0, 25, 100) samples were carried out on a Bruker 500 MHz (11.7 T) spectrometer equipped with a 2.5 mm MAS probe, operating at a Larmor frequency of 132.294 MHz. Approximately 18 mg of sample was packed into a 2.5 mm zirconia rotor for each measurement. ^{23}Na spectra were acquired using a single-pulse experiment with a π/2 pulse length of 3.79 μs, a recycle delay of 50 s, and a spinning rate of 25 kHz. Spin-lattice relaxation times (T_1) were measured using an inversion-recovery pulse sequence. The ^{23}Na spectra are referenced to solid NaCl at 7.2 ppm. All data was processed and extracted using TopSpin software. NaCl content was quantified using an external NaCl standard for all samples. The NaCl wt% was calculated from the ratio of integrated NaCl peak areas in the sample and the standard, scaled by their respective masses. All spectra were acquired under identical experimental conditions. Variable-temperature NMR (VT-NMR) was performed to correlate ^{23}Na T_1 relaxation behavior with Na-ion dynamics and motional rates. According to the Bloembergen-Purcell-Pound (BPP) theory (Eq. 2), the spin-lattice T_1 relaxation relates to the motional correlation time (τ_c)[67,68].

The ^{23}Na spin-lattice relaxation behavior was analyzed according to

$$\frac{1}{T_1} = \frac{3}{200}Q_c\left(1 + \frac{\eta^2}{3}\right) \times \frac{2I+3}{I^2(2I-1)}\left[\frac{\tau_c}{1+\omega_0^2\tau_c^2} + \frac{4\tau_c}{1+4\omega_0^2\tau_c^2}\right], \quad (3)$$

where I denotes the nuclear spin quantum number (I = 3/2 for ^{23}Na), Q_c is the nuclear quadrupolar coupling constant, η represent the asymmetric parameter, ω_0 is the Larmor angular frequency, and τ_c is to the motional correlation time. Temperature-dependent ^{23}Na NMR spectra were acquired by an inversion-recovery experiment on a Bruker Avance-I spectrometer operated at 7.05 T (300 MHz), giving a ^{23}Na resonance frequency of 79.35 MHz. During the measurements, the samples were spun at 10 kHz in 4-mm zirconia rotors. Data were collected over the temperature range of 25–65 °C with a 10 °C step. Solid NaCl was used as the chemical-shift reference, with its ^{23}Na resonance assigned to 7.2 ppm. ^{13}C MAS NMR experiments were performed on a Bruker Avance-I NMR spectrometer (300 MHz, 7.05 T) at a Larmor frequency of 75.43 MHz, and a spinning rate of 10 kHz. ~120 mg of sample was packed in a 4 mm zirconia rotor. ^{13}C shift was calibrated using ADA at 38.48 ppm.

Mechanical property measurements

Elastic modulus and hardness were evaluated with an Agilent G200 nanoindentation system housed in an argon-filled glovebox, with a three-sided pyramidal diamond Berkovich tip having an effective cone angle of 70.3°. Tests were carried out in continuous stiffness measurements (CSM) mode under depth control, with a fixed indentation strain rate. In this approach, the contact stiffness (S) is determined as a function of indentation depth (h_c) by superimposing a small oscillatory component on the applied load, expressed as $P = P_0e^{i\omega t}$. The resulting displacement response, $h_c = h_0e^{i\omega t+\varphi}$, including its amplitude and phase shift, was simultaneously monitored using a lock-in amplifier[69]. Each test was carried to a maximum indentation depth of 5 μm, chosen so that surface roughness would not affect the measured modulus and hardness. Testing was conducted in a strain-rate of 0.05 s^{-1} with a harmonic displacement amplitude of 1 nm. Sixteen indents were placed in the middle region of each pellet as a 4 × 4 square grid with a 200 μm pitch. Elastic modulus and hardness were calculated from the continuous load, displacement and stiffness data following the Oliver & Pharr analysis[70]. The hardness H is calculated by

$$H = \frac{P_{max}}{A}, \quad (4)$$

where P_{max} is the peak load and A is the projected contact area at that load. Reduced elastic modulus can be obtained from

$$E_r = \frac{\sqrt{\pi}S}{2\beta\sqrt{A}}, \quad (5)$$

in which $\beta = 1.034$ is the geometric correction factor of the Berkovich indenter, A is computed from a tip area function calibrated on a fused silica reference sample using the Oliver & Pharr method. To study time-dependent mechanical properties of the sample, the indentation creep tests were performed. In a creep experiment, a precisely shaped three-sided pyramidal diamond Berkovich indenter is used to probe the time-dependent mechanical behavior of materials under constant load with high-resolution displacement and load sensors. The loading and unloading rate for this measurement was 10 mN s^{-1}, the dwell time is 1000 s, and the indenter was held at peak load of 150 mN during dwell time for all tests. A total of 9 indents were measured at different locations to check the homogeneity of the sample.

Conductivity measurements

The powder samples (150 mg) were cold pressed in a PEEK cell with a diameter of a half inch under 360 MPa to form a dense pellet for conductivity measurements. EIS measurements were performance on the pressed samples using a potentiostat (Biologic SP300) within a frequency range of 5 MHz to 1 Hz. The EIS measurement was conducted with an amplitude of 100 mV, and eight data points were collected per frequency decade. The ionic conductvity was calculated following the equation of

$$\sigma_{Na^+} = \frac{L}{A \times R}, \quad (6)$$

where σ_{Na^+}, L, A and R represent the ionic conductivity (S cm^{-1}), thickness (cm), cross-sectional area (cm^2) and impedance (Ω), respectively. The electronic conductivity of SEs was measured by polarizing under different potentials (−0.3, −0.1, 0.1 and 0.3 V, respectively) for 1 h. The stabilized current was plotted versus potential to obtain the linear fitting slope. The electronic conductvity was calculated following the equation of

$$\sigma_e = \left(\frac{I}{V}\right) \times \left(\frac{L}{A}\right) = slope \times \left(\frac{L}{A}\right), \quad (7)$$

where the *I*, *V*, slope, L and A represent the stable current, polarization potential, slope of *I* vs *V* fitting result, thickness and area, respectively.

Electrochemical measurements

To evaluate the electrochemical stability window of SEs, LSV was employed with Na-Sn as the reference electrode, and NPS as anolyte. For positive scanning, the positive electrode composite was prepared by mixing NZC-yCO sample with acetylene black with a mass ratio of 90:10. For negative scanning, the positive electrode composite was prepared by mixing NZC-yCO with aluminum powder with a mass ratio of 80:20. The scanning rate is 0.1 mV s^{-1} and the positive and negative scanning limit are 6 V and 0 V, respectively.

All-solid-state batteries (ASSBs) were assembled in PEEK cells (a diameter of 1/2-inch) with the configuration of Na-Sn|NPS | NZC-yCO| composite positive electrode ($y = 0$, 100). The composite positive electrode was prepared by mixing $NaCrO_2$ (NEI Corporation), SE and vapor-grown carbon fiber in a weight ratio of 40:58:2, and the active positive electrode loading was 5 mg cm^{-2} (6.4 mg of active positive electrode for the cell with a 0.5-inch diameter). All the ASSBs were tested under a stack pressure of ~70 MPa. The galvanostatic charge-discharge test was conducted on the NEWARE testing system. All sample handling and assembly were performed inside a glovebox with controlled H_2O and O_2 levels.

Preliminary materials cost analysis

The laboratory-scale prices of precursors are mostly taken from Thermo Fisher Chemicals except that $ZrCl_4$, $HfCl_4$, ZrF_4 and NaF are from Fisher Scientific. (Note: the chemicals with lowest purity were selected for estimation, and price is based on 2025 September).

Data availability

The data that support the findings of this study are available within the Article and its Supplementary Information. Source data are provided with this paper. All other relevant data that support the findings of this study can be obtained from the corresponding authors upon request. Source data are provided with this paper.

References

1. Zhao, C. et al. Solid-state sodium batteries. *Adv. Energy Mater.* **8**, 1703012 (2018).
2. Yang, P. et al. Engineering ion transport in all-solid-state sodium-ion batteries: fundamentals, strategies, and perspectives. *Prog. Mater. Sci.* **154**, 101503 (2025).
3. Yang, Y. et al. Inorganic all-solid-state sodium batteries: electrolyte designing and interface engineering. *Adv. Mater.* **36**, 2308332 (2024).
4. Guo, X., Halacoglu, S., Chen, Y. & Wang, H. Recent progress on dominant sulfide-type solid-state Na superionic conductors for solid-state sodium batteries. *Small* **20**, 2311195 (2024).
5. Wu, M. et al. Structure designing, interface engineering, and application prospects for sodium-ion inorganic solid electrolytes. *InfoMat* **6**, e12606 (2024).
6. Wang, C., Liang, J., Kim, J. T. & Sun, X. Prospects of halide-based all-solid-state batteries: from material design to practical application. *Sci. Adv.* **8**, eadc9516 (2022).
7. Tao, B., Zhong, D., Li, H., Wang, G. & Chang, H. Halide solid-state electrolytes for all-solid-state batteries: structural design, synthesis, environmental stability, interface optimization and challenges. *Chem. Sci.* **14**, 8693–8722 (2023).
8. Asano, T. et al. Solid halide electrolytes with high lithium-ion conductivity for application in 4 V class bulk-type all-solid-state batteries. *Adv. Mater.* **30**, 1803075 (2018).
9. Wu, E. A. et al. A stable cathode-solid electrolyte composite for high-voltage, long-cycle-life solid-state sodium-ion batteries. *Nat. Commun.* **12**, 1256 (2021).
10. Schlem, R., Banik, A., Eckardt, M., Zobel, M. & Zeier, W. G. Na3−xEr1−xZrxCl6—a halide-based fast sodium-ion conductor with vacancy-driven ionic transport. *ACS Appl. Energy Mater.* **3**, 10164–10173 (2020).
11. Wang, S. et al. Design principles for sodium superionic conductors. *Nat. Commun.* **14**, 7615 (2023).
12. Kwak, H. et al. Na2ZrCl6 enabling highly stable 3 V all-solid-state Na-ion batteries. *Energy Storage Mater.* **37**, 47–54 (2021).
13. Huang, Z., Yoshida, S., Akamatsu, H., Hayashi, K. & Ohno, S. NaMCl6 (M = Nb and Ta): a new class of sodium-conducting halide-based solid electrolytes. *ACS Mater. Lett.* **6**, 1732–1738 (2024).
14. Park, J. et al. NaAlCl4: new halide solid electrolyte for 3 V stable cost-effective all-solid-state Na-ion batteries. *ACS Energy Lett.* **7**, 3293–3301 (2022).
15. Sebti, E. et al. Synthetic control of structure and conduction properties in Na–Y–Zr–Cl solid electrolytes. *J. Mater. Chem. A* **10**, 21565–21578 (2022).
16. Li, Y. et al. Halide solid-state electrolytes for all-solid-state sodium batteries: progress and perspectives. *ACS Energy Lett.* **10**, 5520–5541 (2025).

17. Fu, C. et al. LaCl3-based sodium halide solid electrolytes with high ionic conductivity for all-solid-state batteries. *Nat. Commun.* **15**, 4315 (2024).
18. Ridley, P. et al. Amorphous and nanocrystalline halide solid electrolytes with enhanced sodium-ion conductivity. *Matter* **7**, 485–499 (2024).
19. Li, L. et al. Highly stable and encapsulation-microstructural cathode derived by self-pressurization behavior in Na-halides-based all-solid-state batteries. *Energy Storage Mater.* **63**, 103016 (2023).
20. Dai, T. et al. Inorganic glass electrolytes with polymer-like viscoelasticity. *Nat. Energy* **8**, 1221–1228 (2023).
21. Lin, X. et al. A dual anion chemistry-based superionic glass enabling long-cycling all-solid-state sodium-ion batteries. *Angew. Chem.* **136**, e202314181 (2024).
22. Zhao, T. et al. Sodium metal oxyhalides NaMOCl4 (M = Nb, Ta) with high ionic conductivities. *ACS Mater. Lett.* **6**, 3683–3689 (2024).
23. Motohashi, K., Tsukasaki, H., Mori, S., Sakuda, A. & Hayashi, A. Fast sodium-ion conducting amorphous oxychloride embedding nanoparticles. *Chem. Mater.* **36**, 9914–9921 (2024).
24. Ojelade, I. A. et al. Break it down to speed it up: Na2O–NaTaCl6. *Chem. Sci.* **16**, 19857–19866 (2025).
25. Wang, X. et al. A new class of carbonate–oxychloride solid electrolytes for high-performance sodium-ion all-solid-state batteries. *Energy Environ. Sci.* **18**, 9927–9938 (2025).
26. Kwak, H. et al. Boosting the interfacial superionic conduction of halide solid electrolytes for all-solid-state batteries. *Nat. Commun.* **14**, 2459 (2023).
27. Guo, X., Chen, Y., Yu, D. & Wang, H. Aliovalent anion incorporation in halide Na-ion conductors for enhanced ionic conductivity. *ACS Energy Lett.* **11**, 3242–3249 (2026).
28. Wu, M. et al. Fluorinated amorphous halides with improved ionic conduction and stability for all-solid-state sodium-ion batteries. *Nat. Commun.* **16**, 2808 (2025).
29. Hu, Y. et al. Superionic amorphous NaTaCl6 halide electrolyte for highly reversible all-solid-state Na-ion batteries. *Matter* **7**, 1018–1034 (2024).
30. Willis, B. T. M. & Carlile, C. J. *Experimental Neutron Scattering* (Oxford University Press, 2017).
31. Dong, Z. L. et al. Novel sulfide-chloride solid-state electrolytes with tunable anion ratio for highly stable solid-state sodium-ion batteries. *Adv. Mater.* **37**, 2503107 (2025).
32. Koller, H., Engelhardt, G., Kentgens, A. P. & Sauer, J. 23Na NMR spectroscopy of solids: interpretation of quadrupole interaction parameters and chemical shifts. *J. Phys. Chem.* **98**, 1544–1551 (1994).
33. Kipouros, G. J. & Flengas, S. N. Equilibrium decomposition pressures of the compounds Na2ZrCl6 and Na2HfCl6. *Can. J. Chem.* **59**, 990–995 (1981).
34. Li, J. et al. Rational design of porous nest-like basic Co-Ni carbonates on carbon cloth with optimized electrode process for efficient electrochemical energy storage. *Nano Energy* **128**, 109954 (2024).
35. Foradori, S. M. et al. Selective oxidation and removal of hydrocarbons from carbon nanotubes using reactive yttrium films. *Carbon* **231**, 119709 (2025).
36. Singh, B. et al. Critical role of framework flexibility and disorder in driving high ionic conductivity in LiNbOCl4. *J. Am. Chem. Soc.* **146**, 17158–17169 (2024).
37. Huang, Z. et al. Oxygen-mediated structural modulation and ion transport in xNa2O-TaCl5 glass electrolytes. *J. Am. Chem. Soc.* **147**, 43391–43399 (2025).
38. Leifeld, J. et al. Disorder-driven fast Na+ transport: From crystalline to amorphous networks in the mixed-anion NaTaOxCl6−2x oxychlorides. *ChemRxiv* https://doi.org/10.26434/chemrxiv-2025-27tgk (2025).
39. Dybowski, C., Bai, S. & Bramer, S. V. Solid-state nuclear magnetic resonance. *Anal. Chem.* **74**, 2713–2718 (2002).
40. Kuhn, A. et al. NMR relaxometry as a versatile tool to study Li ion dynamics in potential battery materials. *Solid State Nucl. Magn. Reson.* **42**, 2–8 (2012).
41. Pharr, G. M. & Oliver, W. C. Measurement of thin film mechanical properties using nanoindentation. *MRS Bull.* **17**, 28–33 (1992).
42. Lin, X. et al. A family of dual-anion-based sodium superionic conductors for all-solid-state sodium-ion batteries. *Nat. Mater.* **24**, 83–91 (2025).
43. Hempel, J. L. et al. Probing the elastic modulus and hardness of superionic boron cluster solid electrolytes. *J. Power Sources* **641**, 236800 (2025).
44. Papakyriakou, M. et al. Mechanical behavior of inorganic lithium-conducting solid electrolytes. *J. Power Sources* **516**, 230672 (2021).
45. Chi, X. et al. An electrochemically stable homogeneous glassy electrolyte formed at room temperature for all-solid-state sodium batteries. *Nat. Commun.* **13**, 2854 (2022).
46. Yu, S. et al. Elastic properties of the solid electrolyte Li7La3Zr2O12 (LLZO). *Chem. Mater.* **28**, 197–206 (2016).
47. Herbert, E. G., Tenhaeff, W. E., Dudney, N. J. & Pharr, G. M. Mechanical characterization of LiPON films using nanoindentation. *Thin Solid Films* **520**, 413–418 (2011).
48. Wolfenstine, J., Go, W., Kim, Y. & Sakamoto, J. Mechanical properties of NaSICON: a brief review. *Ionics* **29**, 1–8 (2023).
49. Han, X. et al. Mechanically robust halide electrolytes for high-performance all-solid-state batteries. *Nat. Commun.* **16**, 9770 (2025).
50. Chen, Z. et al. Low-pressure operation of all-solid-state batteries enabled by low-hardness creep-prone electrodes. *ChemRxiv* https://doi.org/10.26434/chemrxiv-2025-0fvvk (2025).
51. Zhang, J. et al. Configuration design and interface reconstruction to realize the superior high-rate performance for sodium layered oxide cathodes. *Adv. Energy Mater.* **15**, 2405951 (2025).
52. Li, H. et al. Averting irreversible transition metal migration in O3-type NaCrO2 via oxygen vacancy defects to enable durable sodium storage. *Chem. Eng. Sci.* **306**, 121308 (2025).
53. Hart, P. W. & Sommerfeld, J. T. Cost estimation of specialty chemicals from laboratory-scale prices. *Cost. Eng.* **39**, 31 (1997).
54. Fu, J. et al. Halide heterogeneous structure boosting ionic diffusion and high-voltage stability of sodium superionic conductors. *Adv. Mater.* **36**, 2308012 (2024).
55. Zhou, L., Bazak, J. D., Li, C. & Nazar, L. F. 4 V Na solid state batteries enabled by a scalable sodium metal oxyhalide solid electrolyte. *ACS Energy Lett.* **9**, 4093–4101 (2024).
56. Hu, L. et al. Overcoming the Na-ion conductivity bottleneck for the cost-competitive chloride solid electrolytes. *J. Energy Chem.* **95**, 1–8 (2024).
57. Kmiec, S., Ruoff, E. & Manthiram, A. A new class of oxyhalide solid electrolytes NaNbCl6-2xOx for solid-state sodium batteries. *Angew. Chem. Int. Ed.* **64**, e202416979 (2025).
58. Wang, L. et al. Na2.5Cr0.5Zr0.5Cl6: a new halide-based fast sodium-ion conductor. *Small* **20**, 2400195 (2024).
59. Park, J. et al. Extending the electrochemical window of Na+ halide nanocomposite solid electrolytes for 5 V-class all-solid-state Na-Ion batteries. *ACS Energy Lett.* **9**, 2222–2230 (2024).
60. An, K., Chen, Y. & Stoica, A. D. VULCAN: a "hammer" for high-temperature materials research. *MRS Bull.* **44**, 878–885 (2019).
61. An, K. Data reduction and interactive visualization software for event mode neutron diffraction. *ORNL Rep.* **621**, ORNL-TM-2012 (2012).
62. Larson, A. C. & Dreele, R. B. General Structure Analyst System. *Los Alamos National Laboratory Report* 86-748 (2004).

63. Toby, B. H. EXPGUI, a graphical user interface for GSAS. *Appl. Crystallogr.* **34**, 210–213 (2001).
64. Chen, T.-C., Chen, Y., Yu, D., Amalia, L. & An, K. High-temperature neutron diffraction study of vanadium and vanadium–niobium null-matrix alloy for spectrum normalization. *ACS Appl. Eng. Mater.* **3**, 4668–4682 (2025).
65. Liu, J., He, L., Osti, N. C. & Zhang, Y. Neutron scattering in sodium-ion battery research: progress and prospects. *Adv. Energy Mater.* e06774 https://doi.org/10.1002/aenm.202506774 (2026).
66. Zhang, Y., Liu, J. & Tucker, M. G. Lorentz factor for time-of-flight neutron Bragg and total scattering. *Acta Crystallogr. Sect. A* **79**, 20–24 (2023).
67. Bloembergen, N., Purcell, E. M. & Pound, R. V. Relaxation effects in nuclear magnetic resonance absorption. *Phys. Rev.* **73**, 679–712 (1948).
68. Amanchukwu, C. V. et al. Understanding lithium-ion dynamics in single-ion and salt-in-polymer perfluoropolyethers and polyethyleneglycol electrolytes using solid-state NMR. *Macromolecules* **56**, 3650–3659 (2023).
69. Pethica, J. B. & Oliver, W. C. Mechanical properties of nanometre volumes of material: use of the elastic response of small area indentations. *MRS Proc.* **130**, 13 (1988).
70. Oliver, W. C. & Pharr, G. M. An improved technique for determining hardness and elastic modulus using load and displacement sensing indentation experiments. *J. Mater. Res.* **7**, 1564–1583 (1992).

Acknowledgements

The authors (H.W., X.G., M.C.) thank the support from U.S. National Science Foundation CAREER Award (No. 2047460). J.B., T.M., and Y.S.M. acknowledge the support of the Energy Storage Research Alliance "ESRA" (DE-AC02-06CH11357), an Energy Innovation Hub funded by the U.S. Department of Energy, Office of Science, Basic Energy Sciences. S.T. and Y.T.C. would like to thank University of Kentucky for partial financial support. This research used resources at Spallation Neutron Source; a DOE Office of Science User Facility operated by the Oak Ridge National Laboratory. The beam time was allocated to VULCAN and NOMAD on proposal number IPTS-34624 and IPTS-38431, respectively. A portion of this work was performed at the National High Magnetic Field Laboratory, which is supported by National Science Foundation Cooperative Agreement No. DMR-2128556 and the State of Florida. Y.-Y.H. and I.O. acknowledge the support from the National Science Foundation under grant no. DMR-2319151 and would like to thank Dr. J. S. Raaj Vellore Winfred for his technical assistance at the Materials Characterization Laboratory, Florida State University Department of Chemistry and Biochemistry (FSU075000MAC).

Author contributions

H.W. and X.G. conceived the study and designed the experiments. X.G. and M.C. performed the material synthesis, ionic conductivity measurements, structural characterization, neutron Rietveld refinement, and electrochemical testing, supervised by H.W. J.B., M.N., and T.M. performed the capillary XRD measurements and HR-TEM characterization and analysis, supervised by Y.S.M. S.T. performed the mechanical measurements and analysis, supervised by Y.T.C. Y.C. contributed to the neutron diffraction measurements and analysis. I.O., S.H. and R.Z. performed the NMR measurements and analysis, supervised by Y.Y.H. J.L. contributed to the neutron PDF measurements and analysis. H.W., X.G., and M.C. wrote the original manuscript draft, and all authors contributed to data interpretation, discussion of the results, and review and editing of the manuscript.

Funding

H.W., X.G., M.C. disclose support for the research of this work from U.S. National Science Foundation, Directorate for Engineering, CBET Division [grant number 2047460], and support for publication of this work from University of Louisville Research Foundation. J.B., T.M, and Y.S.M. disclose support for the research of this work and support for publication of this work from Energy Storage Research Alliance "ESRA" [grant number DE-AC02-06CH11357], an Energy Innovation Hub funded by U.S. Department of Energy, Office of Science, Basic Energy Sciences. Y.-Y.H., I.O., S.H., and R.Z. disclose support for the research of this work from U.S. National Science Foundation [grant number DMR-2128556; DMR-2319151]. S.T., Y.C., J.L., Y-T.C. declare no relevant funding.

Competing interests

H.W., X.G., M.C., and Y.S.M., J.B., M.N. declared that a joint patent disclosure related to this work was filed through the Office of Research and Innovation at the University of Louisville, and the Polsky Center for Entrepreneurship and Innovation at the University of Chicago. The remaining authors declare no competing interests.

Additional information

Supplementary information The online version contains supplementary material available at https://doi.org/10.1038/s41467-026-79386-9.

Correspondence and requests for materials should be addressed to Y. Shirley Meng or Hui Wang.

Peer review information *Nature Communications* thanks Xabier Martinez de Irujo-Labalde and the other, anonymous, reviewers for their contribution to the peer review of this work. A peer review file is available.

Reprints and permissions information is available at http://www.nature.com/reprints

Publisher's note Springer Nature remains neutral with regard to jurisdictional claims in published maps and institutional affiliations.

Open Access This article is licensed under a Creative Commons Attribution-NonCommercial-NoDerivatives 4.0 International License, which permits any non-commercial use, sharing, distribution and reproduction in any medium or format, as long as you give appropriate credit to the original author(s) and the source, provide a link to the Creative Commons licence, and indicate if you modified the licensed material. You do not have permission under this licence to share adapted material derived from this article or parts of it. The images or other third party material in this article are included in the article's Creative Commons licence, unless indicated otherwise in a credit line to the material. If material is not included in the article's Creative Commons licence and your intended use is not permitted by statutory regulation or exceeds the permitted use, you will need to obtain permission directly from the copyright holder. To view a copy of this licence, visit http://creativecommons.org/licenses/by-nc-nd/4.0/.

© The Author(s) 2026

This Article in Press is shared early to give you faster access to new research. It is citable and carries a permanent DOI. The final edited version will replace it automatically.